Impaired polyamine metabolism causes behavioral and neuroanatomical defects in a novel mouse model of Snyder-Robinson Syndrome

Oluwaseun Akinyele[1], Anushe Munir[1,2], Marie Johnson[1], Megan E. Perez[1,2], Yuan Gao[3], Jackson R. Foley[4], Yijen Wu[5], Tracy Murray-Stewart[4], Robert Casero Jr.[4], Hulya Bayir[3], Dwi U. Kemaladewi[1,2]

[1]Div. of Genetic and Genomic Medicine, Dept. of Pediatrics, University of Pittsburgh School of Medicine, Pittsburgh, USA.

[2]Dept. of Human Genetics, School of Public Health, University of Pittsburgh, Pittsburgh, USA.

[3]Children's Neuroscience Institute, Dept. of Pediatrics, University of Pittsburgh School of Medicine, Pittsburgh, USA.

[4]Sidney Kimmel Comprehensive Cancer Center, Johns Hopkins School of Medicine, Baltimore, Maryland, USA.

[5]Dept. of Developmental Biology, University of Pittsburgh School of Medicine, Pittsburgh, USA.

Corresponding author:

Dwi U. Kemaladewi, Ph.D.

Department of Pediatrics, University of Pittsburgh School of Medicine

UPMC Children's Hospital of Pittsburgh

4401 Penn Ave, Pittsburgh, PA 15224 USA

Dwi.kemaladewi@chp.edu

Abstract

Polyamines (putrescine, spermidine, and spermine) are essential for cellular growth and are subject to strict metabolic regulation. Mutations in the gene encoding spermine synthase (SMS) lead to the accumulation of spermidine and an X-linked recessive disorder known as Snyder-Robinson syndrome (SRS). There are no treatments available for this rare disease that manifests as mental retardation, thin habitus, and low muscle tone. The development of therapeutic interventions for SRS will require a suitable disease-specific animal model that recapitulates many of the abnormalities observed in these patients.

Here, we characterize the molecular, behavioral, and neuroanatomical features of a mouse model with a missense mutation in *Sms* that results in a glycine-to-serine substitution at position 56 (G56S) of the SMS protein. Mice harboring this mutation exhibited a complete loss of SMS protein and elevated spermidine/spermine ratios in skeletal muscles and the brain. In addition, the G56S mice demonstrated increased anxiety, impaired learning, and decreased explorative behavior in fear conditioning, Morris water maze, and open field tests, respectively. Furthermore, the mice undergo significant reductions in body weight over time, as well as abnormalities in brain structure and bone density. Transcriptomic analysis of the cerebral cortex revealed downregulation of genes associated with mitochondrial oxidative phosphorylation and synthesis of ribosomal proteins. Our findings also revealed impaired mitochondrial bioenergetics in fibroblasts isolated from the G56S mice, which provides a link between these processes and the pathogenesis of SRS. Collectively, our findings establish the first in-depth characterization of SRS-associated mechanisms in a preclinical animal model and identify cellular processes that can be targeted for future therapeutic development.

Keywords: Polyamines, Spermine synthase, spermine, neurological, disease, pathogenesis**.**

Introduction

46

47 Putrescine, spermidine, and spermine are ubiquitous polyamines that are essential for normal

48 cellular functions. As a group, these polycationic molecules are responsible for maintaining

49 chromatin structure and regulating gene expression and signaling pathways, as well as cell

50 growth and death. Polyamines are also critical contributors to the many processes underlying

51 immune cell activation, wound healing, and general tissue growth and development (1–6).

52 Given their central role in cellular metabolism, the levels of intracellular polyamines are tightly

53 regulated via *de novo* synthesis, interconversion, and transport into and out of cells (Figure 1).

54 Most of the intracellular polyamine pool arises from *de novo* synthesis. The diamine putrescine,

55 which is the main precursor in this pathway, is synthesized from ornithine via the actions of the

56 enzyme ornithine decarboxylase (ODC). Spermidine and spermine are higher-order polyamines

57 derived from putrescine. Spermidine synthase (SPDS) catalyzes the reaction between

58 putrescine and decarboxylated S-adenosylmethionine (dc-SAM) that generates spermidine.

59 Spermine is then synthesized from spermidine and dc-SAM by spermine synthase (SMS).

60 Spermidine and spermine can be converted back to their respective precursors via the actions

61 of spermidine/spermine N^1-acetyltransferase (SSAT) and acetylpolyamine oxidase (APAO).

62 Dysregulation or absence of any of these enzymes alters the homeostatic levels of cellular

63 polyamines. Aberrancies in polyamine metabolism have been implicated in numerous diseases,

64 including cancers, Alzheimer's disease, and Snyder-Robinson Syndrome (SRS) (7–10).

65 SRS (OMIM: 309583) is a rare X-linked intellectual disability syndrome associated with several

66 known deleterious mutations in the *SMS* gene that lead to the loss of spermine synthase

67 enzymatic activity and thus reductions in the intracellular spermine concentration (10). Loss of

68 SMS activity also leads to an accumulation of spermidine and a high spermidine/spermine ratio,

69 which is a biomarker used clinically to diagnose this disorder (10). SRS is characterized by

70 intellectual disability, seizures, and general developmental delay (10–12). Individuals diagnosed

71 with SRS exhibit thin body habitus and low muscle tone (hypotonia); these clinical findings may

72 be apparent in infancy and worsen over time (10,13). Some SRS patients have difficulty walking

73 and may never become ambulatory(11).

74 While a specific mutation in the *SMS* was first identified as the cause of SRS as early as 2003

75 (14), there are still no suitable animal models available to study disease pathophysiology and

76 support the development of effective therapeutic interventions. Previous reports featured a

77 *Drosophila* model in which an appropriate mutation was introduced into the *sms* gene (15) (16).

78 While *Drosophila* models are readily available, many pathogenic factors that are critical to our

79 understanding of vertebrate diseases are not conserved in this species and thus key aspects

80 and mechanisms may be overlooked (17). To address this concern, several groups used *Gy*

81 (*Gyro*) mice to explore the pathogenesis of SRS (17,18). The *Gy* mouse strain features a

82 complete deletion of the *Sms* gene and exhibits several of the abnormalities described in SRS

83 patients, including altered polyamine content, cognitive impairment, and bone abnormalities

84 (19,20). However, in addition to *Sms* deletion, the *Gy* mice also have deletion of the *Phex* gene.

85 *Phex* encodes the phosphate-regulating endopeptidase homolog, which is a protein involved in

86 phosphate transport that has been implicated in the pathogenesis of X-linked

87 hypophosphatemia (19,20). These attributes (i.e., the complete deletion of both *Sms* and *Phex*)

88 complicate the interpretation of many of the abnormalities observed in the *Gy* mice. Thus, this

89 strain is not an ideal model of SRS.
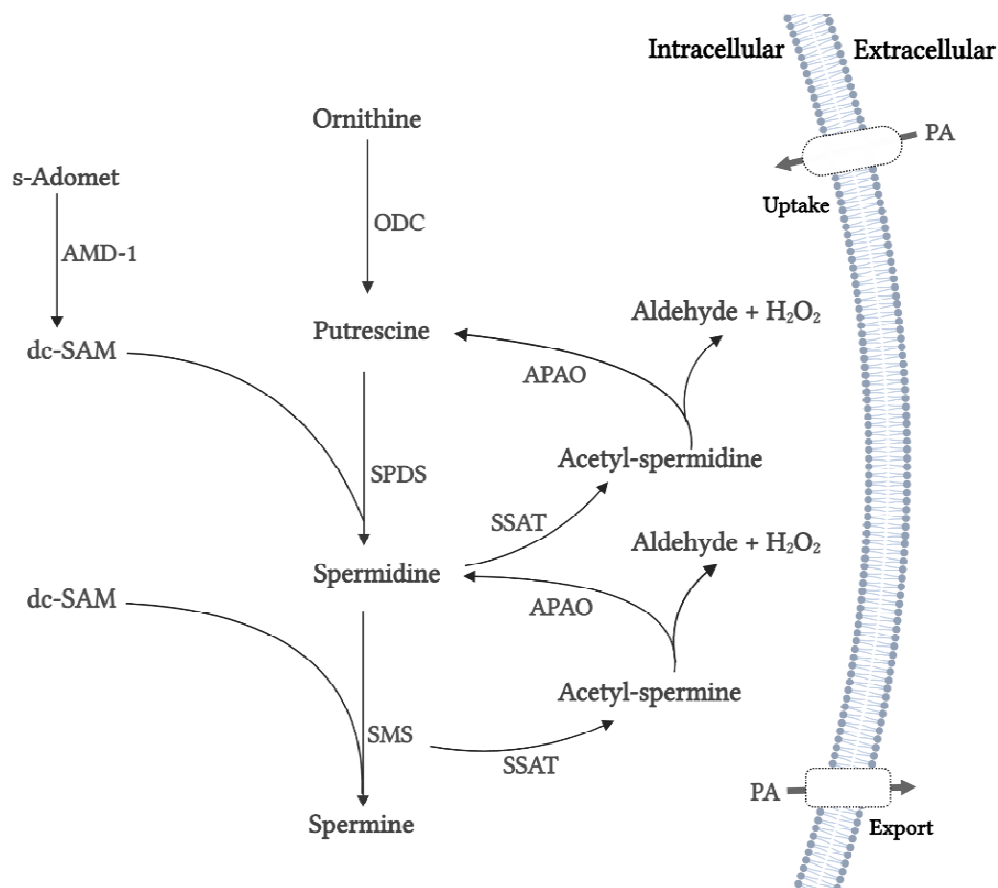
90
91 **Figure 1. The polyamine metabolic pathway**. Abbreviations: ODC, ornithine decarboxylase; SPDS, spermidine
92 synthase; SMS, spermine synthase; s-Adomet, s-adenosylmethionine; AMD-1, adenosylmethionine decarboxylase;
93 dc-SAM, decarboxylated s-adenosylmethionine; APAO, acetylpolyamine oxidase; SSAT, spermidine/spermine
94 acetyltransferase; PAs, polyamines.

95 Here, we explore disease pathogenesis in a recently generated mouse model of human SRS

96 (21) that carries a disease-specific missense mutation in *Sms* gene. This mouse strain harbors

97 a glycine to serine substitution in the amino acid sequence at position 56 of the SMS protein

98 (G56S), analogous to a mutation reported in individuals diagnosed with severe SRS (11). In this

99 study. we characterized the disease presentation in the G56S mice and explored potential

100   mechanisms underlying some of the observed abnormalities. Our findings revealed that G56S

101   mice exhibit many of the phenotypic (both behavioral and neuroanatomical) abnormalities

102   reported in SRS individuals (11,22,23). Furthermore, a transcriptomic analysis identified critical

103   changes in gene expression patterns that might contribute to these observed aberrancies.

104   **Materials and methods**

105   **Mice:** All animals used in this study were housed at the University of Pittsburgh Division of

106   Laboratory Animal Resources, Rangos Research Building, following the IACUC protocol

107   number 2206137, which was approved by the University of Pittsburgh's Institutional Animal

108   Care and Use Committee. The colony of mutant mice was established by breeding female

109   heterozygous *Sms* mutation carriers (C57BL/6J-Sms[em2Lutzy]/J; Jackson Laboratory stock #

110   031170) and male WT C57BL/6J mice (Jackson Laboratory stock # 000664). The male offspring

111   of this cross that harbored the X-linked G56S *Sms* mutation and WT littermate controls were

112   used in the experiments described in this study. To ensure that only male mice harboring the

113   desired mutation were used, pups were genotyped at Transnetyx.com using the following

114   probes: forward   primer   ACCTGGCAGGACCATGGATATTTA,   reverse   primer

115   GTGTTCACATCTAAAGCCCATGAGA, reporter 1 AACAAGAATGGCAGGTAAG, and reporter

116   2 ACGAACAAGAATTCCAGG.

117   **Open field activity assay:** The open field chamber is a hollow square field box equipped with

118   tracking software (ACTITRACK, Panlab/Harvard Apparatus, USA) connected to an infrared

119   tracking system that monitors animal movement. The walls of the box were opacified (covered

120   with aluminum foil) to prevent the environment from influencing the behavior of the mice that

121   were undergoing testing. The chamber was divided into two imaginary zones: an outer zone (45

122   x 45 cm) and an inner or center zone (18.5 cm x 18.5 cm, centered at 22.5 cm from the wall on

123   each side). Experiments were undertaken under constant room temperature ($22 - 25^{O}C$) and

124   light levels. Each mouse was released at the same location near the wall of the box and

125   movement was evaluated for 15 minutes using the infrared tracking system. The positions

126   recorded for each mouse were used to generate tracking plots and to determine the distance

127   traveled, speed, and time spent in each zone (i.e., within the entire apparatus and specifically in

128   the center zone). The total amount of time spent and the type of body motion (i.e., rearing,

129   leaning, and vertical activity) detected in the center zone were used as relative measurements

130   of explorative behavior and anxiety-related responses, respectively.

131   **Auditory-cued fear conditioning:** The conditioning procedure was carried out using a

132   specifically designed chamber (model *H10-11M-TC-SF* Coulbourn Instruments, Whitehall, PA,

133   USA). The conditioning chamber ($25 \times 25 \times 25$ cm) had three grey methacrylate walls, a grid

134   floor connected to a shock scrambler to deliver foot shock as the unconditioned stimulus (US),

135   and a speaker mounted on the chamber ceiling to deliver audible tones as the conditioned

136   stimulus (CS). The conditioning chamber was fitted with a high sensitivity camera system that

137   monitored animal movement. The chamber was confined in a ventilated, soundproof enclosure

138   (78 × 53 × 50 cm) on an anti-vibration table in a quiet room. The door to the room remained

139   closed throughout the conditioning and testing periods.

140   On the first day (fear acquisition), the animals were habituated for 120 sec in the chamber

141   before the delivery of CS-US pairs (i.e., a 75 dB tone [CS] for 20 sec followed by a 15-sec trace

142   and then foot shocks [US] of 0.6 mA for 2 sec) with variable and pseudo-randomly distributed

143   intervals between pairs of stimuli (90 – 203 sec). On the second day (fear retention), the session

144   started with the mice placed in the same environment. During this phase, the mice were

145   provided with no stimulation that might elicit contextual fear responses. Freezing responses in

146   this otherwise familiar environment were monitored.

147   For the third session, the mice were placed in a different environmental setting (i.e., a chamber

148   with a covered floor and white walls) to assess the retention of cued fear in a novel context.

149   Baseline fear responses were monitored for 90 sec followed by the delivery of three CS (75 dB

150   and 20 s) separated by variable inter-trial intervals (ITIs). The movement of the animal was

151   sampled at a frequency of 50 Hz for quantitative analysis (Freezeframe, Coulbourn Instruments,

152   USA). Freezing was analyzed during the delivery of the CS (20 sec periods) as well as during

153   the 15 sec trace period that would ordinarily precede the US (not delivered) to monitor the

154   associative fear response. The animals were gently handled before, during, and after the test to

155   avoid introducing any additional potential stress before or during each test that could influenced

156   the measured responses.

157   **Morris Water Maze (MWM) Task**: The MWM task was performed in a circular pool containing

158   water using the procedure described by Tsien et al. (24) with slight modifications. The animals

159   were trained to find an escape platform that was submerged in the water. The animals were not

160   habituated in the pool before the training. The training protocol (hidden platform, used to

161   evaluate spatial learning) included five sessions with 4 trials per session per day. Navigation

162   was tracked by a video camera and the escape latency (i.e., the time required to locate the

163   platform) was recorded. An animal that failed to locate the platform within 90 sec was guided to

164   the platform. We then performed visible (to measure spatial memory) and probe (to measure

165   non-spatial memory) tests on day six. In the visible test, colored tape was placed at the top of

166   the platform. For the probe test, the platform was removed; the mice were allowed to swim in

167   the pool for 60 s, and the time spent in each quadrant of the pool was recorded. The acquire

168   data was analyzed using the ANY-maze software.

169   ***In vivo* Magnetic Resonance Imaging (MRI) scans:** All mice were subjected to *in vivo* brain

170   imaging while under isoflurane anesthesia. The mice were placed in a clear plexiglass

171   anesthesia induction box that permitted unimpeded visual monitoring. Induction was achieved

172   by the administration of 3% isoflurane in oxygen for several minutes. The depth of anesthesia

173   was monitored by toe reflex (extension of limbs, spine positioning) and respiration rate. Once

174   established, the appropriate level of anesthesia was maintained by continuous administration of

175   1-2 % isoflurane in oxygen via a nose cone. The mice were then transferred to the designated

176   animal bed for imaging. Respiration was monitored using a pneumatic sensor placed between

177   the animal bed and the mouse's abdomen. Rectal temperature was measured with a fiber optic

178   sensor and maintained with a feedback-controlled source of warm air (SA Instruments, Stony

179   Brook, NY, USA).

180   *In vivo* brain MRI was carried out on a Bruker BioSpec 70/30 USR spectrometer (Bruker

181   BioSpin MRI, Billerica, MA, USA) operating at 7-Tesla field strength and equipped with an

182   actively shielded gradient system and a quadrature radio-frequency volume coil with an inner

183   diameter of 35 mm. Multi-planar T_2-weighted anatomical images were acquired with a Rapid

184   Imaging with Refocused Echoes (RARE) pulse sequence with the following parameters: field of

185   view (FOV) = 2 cm, matrix = 256 X 256, slice thickness = 1 mm, in-plane resolution = 78 µm X

186   78 µm, echo time (TE) = 12 msec, RARE factor = 8, effective echo time (ETE) = 48 msec,

187   repetition time (TR) = 1800 msec, and flip angle = 180^0. Multi-planar diffusion MRI was

188   performed using the following parameters: field of view (FOV) = 2.0 cm, matrix = 128 X 128,

189   slice thickness = 1.5 mm, in-plane resolution = 156 µm X 156 µm, TE = 16.31 msec, TR = 1500

190   msec, diffusion preparation with the spin echo sequence, diffusion gradient duration = 4 msec,

191   diffusion gradient separation = 8 msec, diffusion direction = 30, number of A_0 images = 1, and b

192   value = 1500 s/mm^2.

193   The MRI data were exported to a DICOM format and analyzed using the open source ITK-

194   SNAP (http://www.itksnap.org) brain segmentation software by 2 independent observers who

195   were blinded to the experimental conditions. The volumes of each region of interest (ROI),

196   including the amygdala, corpus callosum, thalamus, ventricles, hippocampus, and cortex were

197   manually drawn by blinded observers based on the information obtained from the Allen mouse

198   brain atlas (https://mouse.brain-map.org/static/atlas). To account for potential difference in the

199   sizes of brains in G56S and WT mice, volumes from each brain region were normalized to the

200   total brain volume of each mouse.

Diffusion MRI was analyzed by the open source DSI studio (http://dsi-studio.labsolver.org/) to obtain fractional anisotropy (FA). ROIs contributing to quantitative and statistical analyses, including the cortex, hippocampus, thalamus, corpus callosum, and ventricles with cerebrospinal fluid (CSF) were manually segmented and defined by blinded independent observers.

***In vivo* micro-Computed Tomography (micro-CT) scans**: All mice undergoing *in vivo* micro-CT imaging were maintained under general inhalation anesthesia with isoflurane as described for MRI scans above. Once established, anesthesia was maintained with 1.5% isoflurane in oxygen administered using a nose cone and the mouse was transferred to the designated animal bed for imaging. Respiration was monitored as described above. Respiration gating was performed using BioVet system that was triggered by maximal inhalation with a 500 ms trigger delay.

Respiration-gated *in vivo* micro-CT imaging was performed with Siemens Inveon Multimodality micro-CT-SPECT-PET system with the following parameters: full rotation, 360^0 projections; settle time 1000 msec; 4X4 binning; effective pixel size of 76.75 µm; trans axial field of view (FOV) 78.6 mm with 4096 pixels; axial FOV 76.1 mm with 3968 pixels 80 kV of voltage; current of 500 µA; exposure time of 410 ms. The three-dimensional (3D) micro-CT images were reconstructed using the Feldkamp algorithm and were calibrated in Hounsfield Units (HU). Double distilled water was set at a readout of 0 and air at 1000 HU.

The 3D micro-CT image stacks were analyzed using the Inveon Research Workplace (IRW). The ROI analysis function was used with a thresholding tool that created several ROIs with different Hounsfield Unit (HU). A cylindrical 3D ROI was drawn around the body that encompassed the entire body. All external air around the mouse was excluded from the ROI and a custom threshold was set between 400 – 5700 HU to capture the bones. The mean HU values obtained from each ROI were used to quantify bone density.

Body composition measurements: Body composition (percentage lean and fat weight) of the mice was measured by quantitative MRI (EchoMRI, Echo Medical Systems, Houston, TX). Animals were placed in thin-walled plastic cylinders with a plastic restraining inserts. Each animal was briefly subjected to a low-intensity electromagnetic field that measured total body composition. Percentages of fat and lean body weights were determined based on total body weight.

Primary cell isolation: Primary fibroblast cultures from the ears of G56S and WT mice were established using the protocol described by Khan and Gasser(25).

RNA isolation and quantitative polymerase chain reaction (qPCR): Total RNA was isolated from mouse tissues using the Nucleospin RNA Plus kit (Macherey-Nagel, cat# 740984.50), following the manufacturer's instructions. cDNA synthesis was performed using the iScript Reverse Transcriptase Supermix kit (BioRad, Cat# 1708841) according to the manufacturer's instructions. qPCR was performed using 2X SYBR Green Fast qPCR Mix kit (ABclonal, cat# RM21203) in a C1000 Touch Thermal Cycler (BioRad, USA). The primer sequences used to amplify target sequences of interest are listed in Supplementary **Table 1**. Expression of endogenous *Gapdh* was used as an internal control to measure the relative expression of genes of interest. The $2^{\Delta\Delta Ct}$ was used to assess relative fold change in gene expression in tissue samples from WT and G56S mice samples. Values are presented as the percentage change in fold expression.

RNA-sequencing (RNAseq) and pathway enrichment analysis: After completing the extraction procedure described above, RNA samples were submitted to the Health Sciences Genomic Core at the UPMC Children's Hospital of Pittsburgh. RNA quality was determined using the Agilent Bioanalyzer 2100 (Agilent Technologies). cDNA libraries were prepared using a 3′-Tag-RNA-Seq library kit (Illumina). Sequencing was performed using one lane of a Hi-Seq 4000 platform with pair-end 40 bp reads. Analysis of sequence reads, including quality control, mapping, and generation of tables of differentially expressed genes (DEGs), heatmaps, and volcano plots) were performed using the Qiagen licensed CLC Genomic Workbench software version 22.0.1. Pathway enrichment analysis of the DEGs was performed using the Qiagen-licensed Ingenuity Pathway Analysis (IPA) software. The gene expression profile identified by RNA-seq was validated by qPCR as described above.

***In vivo* analysis of mitochondria respiration:** Oxygen consumption rates (OCRs) were determined with a Seahorse XFe96 Extracellular Flux Bioanalyzer (Agilent Technologies, Santa Clara, California, USA). Primary fibroblasts plated in 96-well assay plate at a density of 40,000 cells/well were cultured overnight and then equilibrated with Seahorse XF base medium (Agilent Technologies) supplemented with glucose, sodium pyruvate, and L-glutamine at 37˚C in a CO_2-free incubator for 1 hour prior to the assay. Mitochondrial function was assessed by sequential addition of 1.5 µM oligomycin, 1 µM FCCP (carbonyl cyanide-4-[trifluoromethoxy] phenylhydrazone), and 0.5 µM rotenone/antimycin A by the Seahorse Bioanalyzer. Data was normalized by the total protein content of the cells.

Protein isolation, quantification, and western blotting. Total proteins were extracted from tissues isolated from G56S and WT mice tissues using RIPA homogenizing buffer (150 µL of 50 mM Tris HCl pH 7.4, 150 nM NaCl, 1 mM EDTA) followed by homogenization using a bullet

268   blender. After homogenization, 150 μL of RIPA double-detergent buffer (2% deoxycholate, 2%

269   NP-40, 2% Triton X-100 in RIPA homogenizing buffer) supplemented with protease inhibitor

270   cocktail (Roche, cat# A32953) was added to the tissue homogenate followed by incubation on a

271   shaker for 1 h at 4^0C. The tissue homogenate was then centrifuged at 11,000 g for 10 min at

272   4^0C. The resulting supernatant was used to quantify total protein using the Pierce BCA protein

273   assay kit (Thermo Scientific, cat# 23225) according to the manufacturer's protocol. Twenty

274   microgram of total protein was fractionated on 4 – 12% gradient gel (Thermo Scientific, cat#

275   NP0336BOX). After proteins had separated on the gel, they were transferred by electroblotting

276   onto a Polyvinylidene fluoride (PVDF) membrane and blocked with 5% non-fat milk in TBS-

277   Tween-20. The membrane was then incubated overnight with rabbit anti-spermine synthase

278   (Abcam, cat# ab156879 [EPR9252B]) or rabbit anti-vinculin (Abcam, cat# ab129002

279   [EPR8185]). After incubation with the primary antibody, the membranes were washed and then

280   incubated with the secondary antibody (Goat Anti-Rabbit IgG – HRP conjugate, Bio-Rad cat#

281   1706515) for one hour at room temperature. Specific protein bands were detected using

282   SuperSignal^{TM} West Femto Maximum Sensitivity Substrate (Thermo Scientific, cat# 34095).

283   Bands corresponding to immunoreactive SMS and Vinculin were identified and quantified using

284   the ChemiDoc Imaging System (BioRad).

285   **Polyamine measurement:** The polyamine content in isolated tissues was measured by the

286   precolumn dansylation, high-performance liquid chromatography method described by Kabra et

287   al. using 1,7-diaminoheptane as the internal standard (26).

288   **Statistical analysis:** Statistical analysis was performed using Graphpad Prism software vs 9.0.

289   Each variable was statistically compared between the WT and G56S mice using unpaired

290   students' t-test unless otherwise stated. A p value less than 0.05 was considered statistically

291   significant.

292

293   **RESULTS**

294   ***Sms* mutation altered the tissue polyamine content in mouse tissues**

295   To determine whether the substitution of two nucleotides (GGC to TCC) in exon two of the *Sms*

296   gene altered its expression profile and tissue polyamine levels, we measured *Sms* mRNA and

297   protein in tissues isolated from bothG56S and WT control mice. While there were no significant

298   changes in the level of *Sms* mRNA (Figure 2a), we observed a near-complete loss of SMS

299   protein in both the brain and skeletal muscles of G56S mice (Figure 2b). Similarly, an LC-MS

300   analysis of tissue polyamines revealed elevated levels of both putrescine and spermidine and a

301   significant decrease in spermine in brain tissue from G56S mice. The spermidine to spermine

302   ratio was 4-times higher in brain tissues from G56S mice compared to WT controls (Figure 2c).

303   Our findings also revealed a significant increase in spermidine but no changes in the putrescine

304   levels in skeletal muscles of the G56S strain (Figure 2d and inset). The spermine concentration

305   was below the limits of detection in the mutant strain. Figure 2e presents the two-dimensional

306   (2D) crystal structure of the dimerized and fully functional SMS protein including the C-terminal

307   (catalytic) and N-terminal (dimerization) domains; the amino acid within the latter domain at

308   position 56 (WT, glycine) is highlighted in Figure 2f. Figure 2g presents the mutant SMS protein

309   with a serine at position 56; the extended side chain characteristic of this amino acid may

310   interfere with monomer dimerization and may lead to the loss of SMS protein despite normal

311   transcript level.
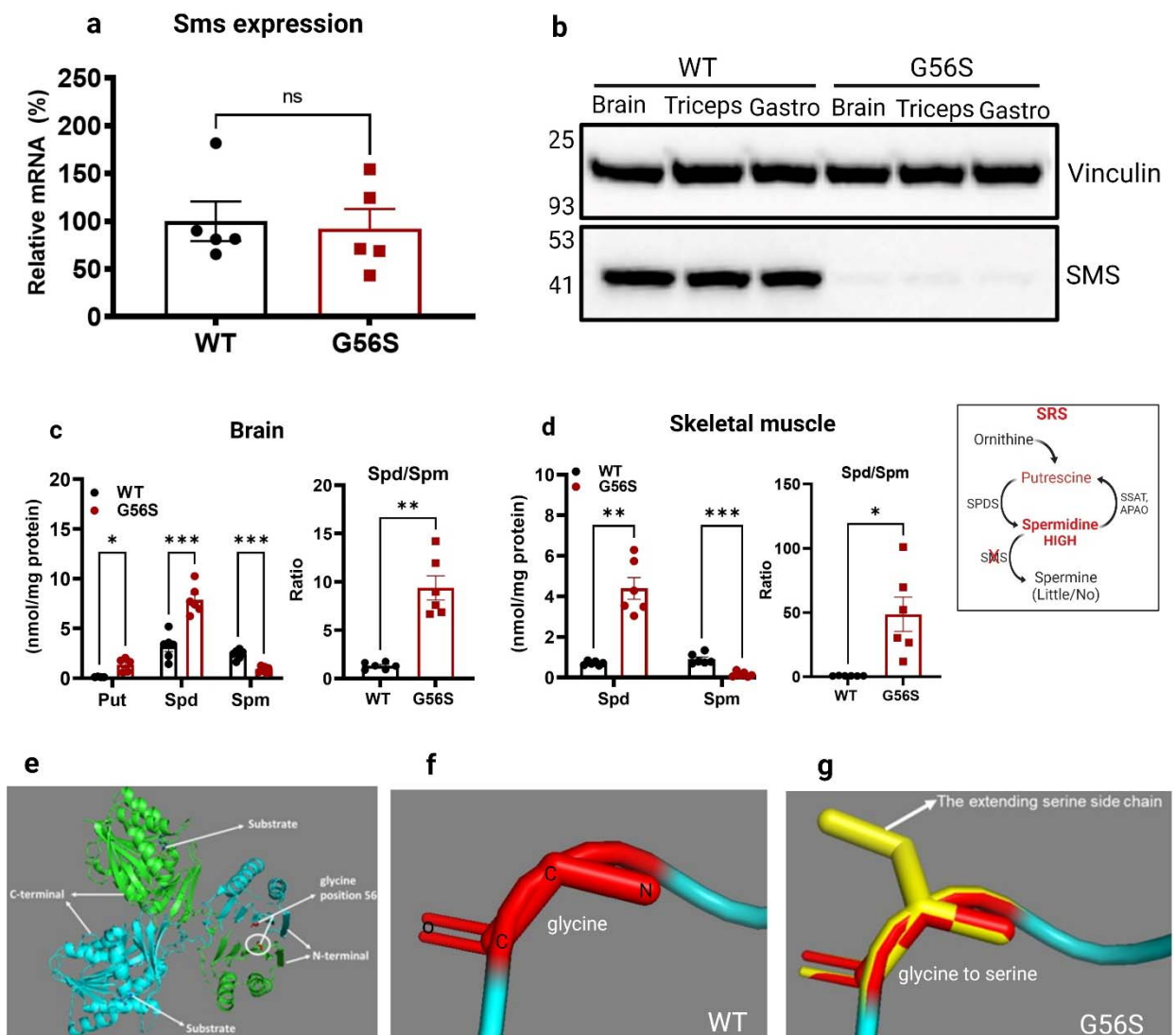
312

313   **Figure 2. Tissue polyamine content and a potential mechanism underlying SMS protein loss**. (a) Mice brain
314   *Sms* gene transcript level as quantified by RT-qPCR. The level of gene transcript in the mutant was compared to the
315   WT mice set at 100% reference value (b) Expression of SMS protein in isolated brain and skeletal muscles (triceps
316   and gastrocnemius) from WT and G56S mice. (c) LC-MS determination of brain polyamine content and SPD/SPM
317   ratios in WT and G56S mice quantified by LC-MS. (d) Skeletal muscle polyamine content in both G56S and WT mice.

318 Note: spermine levels were below the limit of detection in the G56S skeletal muscle. (e) 2D-crystal crystal structure of
319 the SMS protein with glycine at position 56 in the N-terminal region (circled). The 2D-crystal structure SMS was
320 modeled from protein data bank ID: 3C6M. (f) The atomic structure of glycine at position 56 in the N-terminal region
321 of SMS protein. (g) Serine in place of glycine at position 56 of SMS protein; the extended serine sidechain is
322 highlighted in yellow. Panels a-d, values shown are mean ± standard error of the mean (S.E.M.); n = 3 – 5 mice per
323 group; *$p < 0.05$, **$p < 0.01$, ns = not significant.
324

Biometric parameters are significantly altered in G56S mice

Patients diagnosed with SRS typically exhibit an asthenic physique with thin body build and short stature. Many of these patients also exhibit significant bone abnormalities and low muscle tone (10). To understand the mechanisms contributing to these physical aberrations, we determined the impact of altered polyamine content on the growth and development of G56S mice. Routine measurements revealed that the G56S mice have significantly lower body weight than age-matched WT counterparts and that they gained little to no weight throughout the duration of the study period (Figure 3a). Similarly, the G56S mice exhibit significantly reduced body lengths (Figure 3b). Collectively, these results suggest that G56S mice may experience failure to thrive compared to their WT littermates. Also, an analysis of the body composition of mutant mice revealed higher percentage of lean weight and a lower percentage of fat weight compared to their WT counterparts (Figure 3c). This finding may reflect the diminished body build typically observed in patients diagnosed with SRS. Similarly, quantification of bone density by micro-CT revealed that the G56S mice exhibited decreased bone density compared to their WT littermates (Figure 3d). Taken together, these data suggest that changes in tissue polyamine content observed in the G56S mice may have an impact on tissue development and result in general failure to thrive.

342
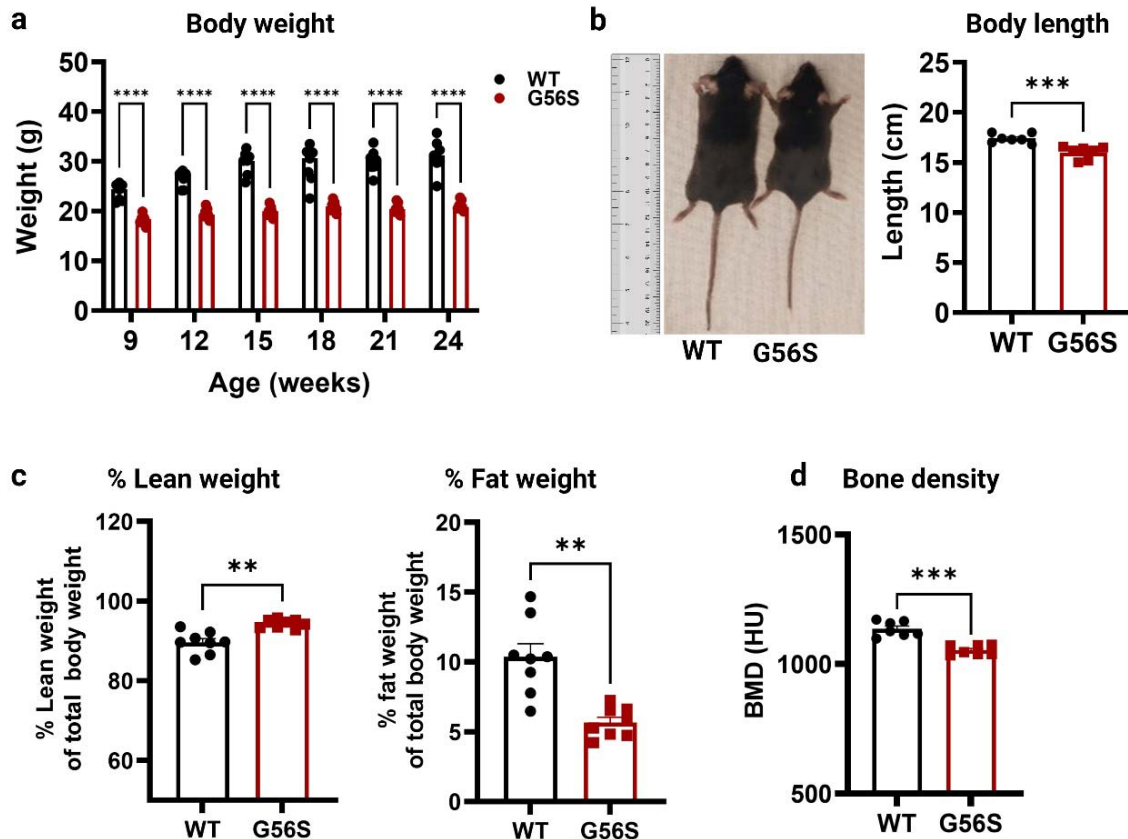
343
344 **Figure 3. Biometric analysis of male G56S and WT mice.** (a) Total body weight was measured in 3-week
345 intervals. (b) Body length of 24-week-old mice. (c) Body composition of 15-week-old mice (% lean and % fat weight)
346 determined by by Echo-MRI scan. (d) Bone mineral density (BMD) of 20-week-old mice measured by micro-CT scan.
347 Values shown are mean ± S.E.M., n = 7 mice per group,** *p < 0.01,* *** *p < 0.001,* **** *p < 0.0001.*

348

349

350 **G56S mice exhibit signs of cognitive impairment**

351 Mild to severe mental retardation is one the major clinical consequences of SRS. Two patients

352 diagnosed with the G56S mutation were reported to have severe cognitive disabilities (11). To

353 explore the impact of the G56S mutation on cognition, we evaluated the performance of G56S

354 and WT mice using the MWM test. For this test, the mice were placed in a pool of water and

355 were provided with five days of training in which they learned to locate an escape platform that

356 was submerged and thus hidden under the water (Figure 4a, panel 1). The time taken to find the

357 platform on each day was recorded.

358 While our findings revealed no significant differences in the time required to find the escape

359 platform, there was a trend suggesting that the WT were somewhat more effective than the

360 G56S mice at performing this task (Figure 4b). Our findings from the probe test in which the

361 platform was completely removed from the MWM (day 6; see Figure 4a, panel 2) revealed no

362 significant differences in the time spent in the escape quadrant (Figure 4c). However, the G56S

363 mice required significantly more time to locate a visible platform (see Figure 4a, panel 3)
364 compared to the WT mice (Figure 4d). This result suggests that the WT mice learned and
365 retained the information needed to complete this task more effectively than the G56S mice.
366 Overall, the results of the MWM test suggest that the G56S mice exhibit relatively mild learning
367 impairments compared to their WT littermates; however, this trait may become more apparent
368 and severe as the mice age.
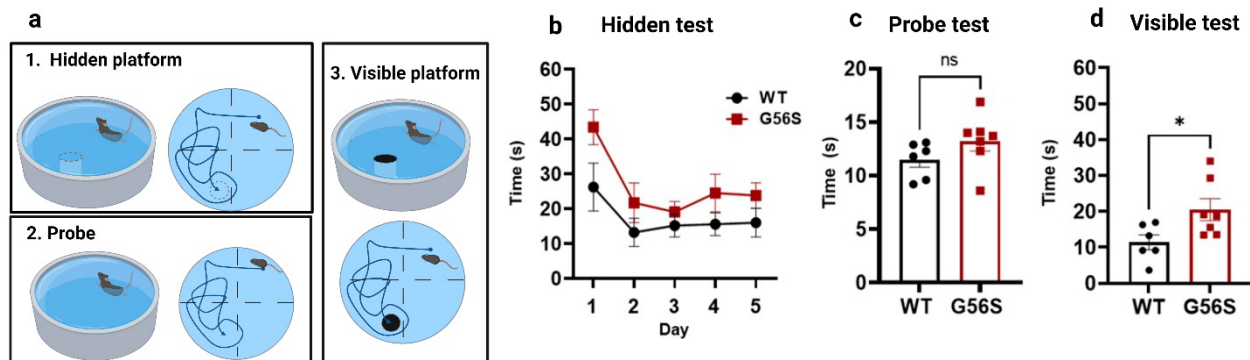
369
370 **Figure 4. Performance of G56S and WT mice in a Morris Water Maze (MWM) test.** (a) Description of the three
371 components of the MWM test. (b) Time required to locate a hidden escape platform on each day of a five-day training
372 period. (c) Time spent in the escape quadrant (probe test without the platform) given a limit of 60 sec on day 6. (d)
373 Time required to locate a visible escape platform on day 6. Data are mean ± s.e.m, n=7 mice per group; two-way
374 ANOVA for repeated measures (a) and unpaired *t*-tests for (b) and (c), not significant (ns); *$p < 0.05$.

G56S mice exhibit diminished explorative behavior in an open field test

376 Anxiety-related responses are among the major symptoms of many neurological and
377 neurodevelopmental disorders, including SRS. Tests designed to evaluate these responses
378 have been used to characterize disease-specific mouse strains. Spontaneous locomotor activity
379 was used to evaluate anxiety-related responses of both G56S and WT mice using a test that
380 provided them with the opportunity to explore an open field arena for 10 min. For this test, the
381 open field arena was divided into an outer or peripheral zone and an inner or center zone
382 (Figure 5a). We assessed the time spent in the center zone, the resting time, and the number of
383 times each mouse entered the center zone. The test was performed once every three weeks to
384 characterize changes in behavior with advancing age.

385 Among our results, we found that the G56S mice were less active compared to their WT
386 counterparts (Figure 5a). While no statistically significant differences were detected between the
387 two strains when the mice were less than 18 weeks old, the G56S mice became significantly
388 less active with increasing age compared to their WT littermates (Figure 5b). Similarly, G56S
389 mice were much less likely to enter the center zone of the open field arena than their WT
390 counterparts beginning at 18 weeks of age (Figure 5c). These results suggest the possibility that
391 the G56S mice experience slow but steady disease progression.

392 Older G56S mice also spent significantly more time resting in the outer zone (Figure 5d) and
393 less time resting in the inner zone of the open field compared to the WT control (Figure 5e).
394 Collectively, these findings suggest that G56S mice exhibit less explorative behavior than their
395 WT counterparts and that these responses may represent higher anxiety or fear that increases
396 as the mice age.
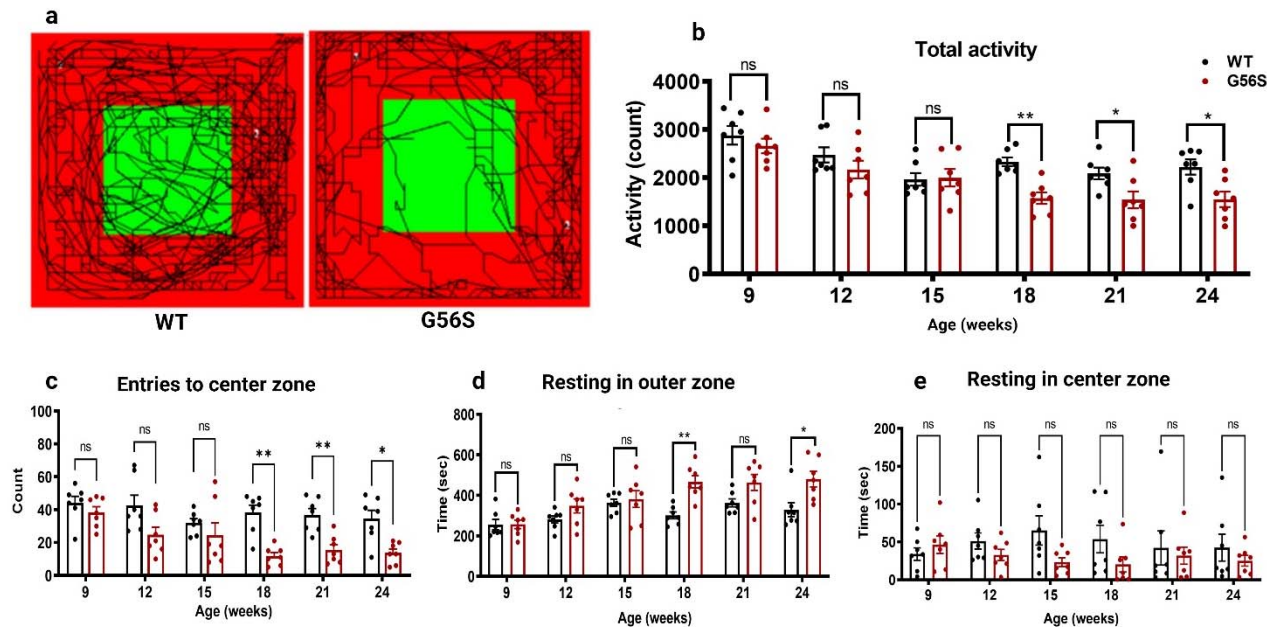
397
398 **Figure 5. Anxiety-related response monitoring in an open field test**. (a) Movement pattern of the animals for 20
399 min in the open field test at 24 weeks of the age. (b) Total activity of the animals in the open field test measured as
400 the number of total numbers of movement, rearing, and other bodily activities. (c) Number of entries to the center
401 zone of the open field test. (d and e) Resting time of the animals in the outer and center zones of the open field
402 respectively. Data are mean ± s.e.m., *$p < 0.05$; **$p < 0.01$; ns, not significant.

403
404
405 **G56S mice exhibit increased fear-related responses**
406 Fear-related responses exhibited by both WT and G56S mice were assessed via
407 measurements of stress-induced freezing. This response is an innate anti-predator fear-related
408 behavior that is characterized by a complete tonic immobilization while sparing respiration. This
409 test uses auditory-cued fear conditioning, which requires the mouse to associate an aversive
410 outcome with an otherwise unrelated cued stimulation.

411 In this experiment, anxiety or fear responses are expressed as the percentage of time spent in a
412 freezing position after sound stimulation (an auditory cue) followed by foot shock (aversive
413 condition).

414 On the first day of the test, the mice were trained to associate the sound (conditioned stimulus,
415 CS) with the foot shock (unconditioned stimulus, US). The percentage of time spent in stress-
416 induced freezing was recorded during the CS and after delivery of the US. We observed a

417 consistent increase in the freezing responses following the CS in both groups of mice; this
418 response reached a plateau after the delivery of the fourth sound stimulation and decreased
419 after the fifth (Figure 6a). These results suggest similar rates of fear acquisition by both groups
420 of mice. However, we observed significant differences in the freezing responses displayed
421 during the inter-trial intervals (i.e., the period between the last foot shock and the next sound
422 stimulation). The G56S mice exhibited significantly longer, and more frequent freezing
423 responses compared to the WT mice (Figure 6b). Similarly, WT mice recovered ambulation
424 more rapidly than the G56S mice following administration of the CS and US. This result
425 indicates that the G56S mice exhibit more profound fear responses following stimulations than
426 their WT counterparts.

427 We then compared the freezing responses of G56S and WT mice in a contextual test. This test
428 was performed 24 hours after the CS-US training and involved no stimulation; the mice were
429 placed in the same experimental chamber and their freezing responses in this environment
430 were measured. While no statistically significant differences were observed, we detected a
431 pattern that suggested that the G56S might exhibit increased freezing responses compared to
432 the WT mice (Figure 6c). This trend suggests that the innate fear responses exhibited by the
433 G56S mice may be more profound when compared to those of their WT littermates.

434 In the cued test, we evaluated the freezing responses of both WT and G56S mice to the CS
435 only in a different environmental setting. After measuring baseline freezing responses during an
436 initial 60 sec habituation period, the mice were subjected to 20 sec of auditory stimulation (CS).
437 Their fear response during the CS and various intertrial intervals were then monitored. While the
438 G56S mice exhibited comparatively higher baseline freezing responses compared to their WT
439 counterparts in the new environmental setting, the differences did not achieve statistical
440 significance. By contrast, the G56S mice exhibited significantly higher fear responses compared
441 to the WT controls both during the CS as well as the ITIs (Figure 6d). Of note, the percentage
442 freezing during the ITIs exhibited by the G56S mice was not only elevated, it remained at a level
443 that was similar to that observed during the CS. Taken together, these data suggest that the
444 G56S mice exhibit higher anxiety-related fear responses than their WT counterparts. This
445 finding may represent a specific neurological dysfunction similar to those observed in patients
446 diagnosed with SRS.
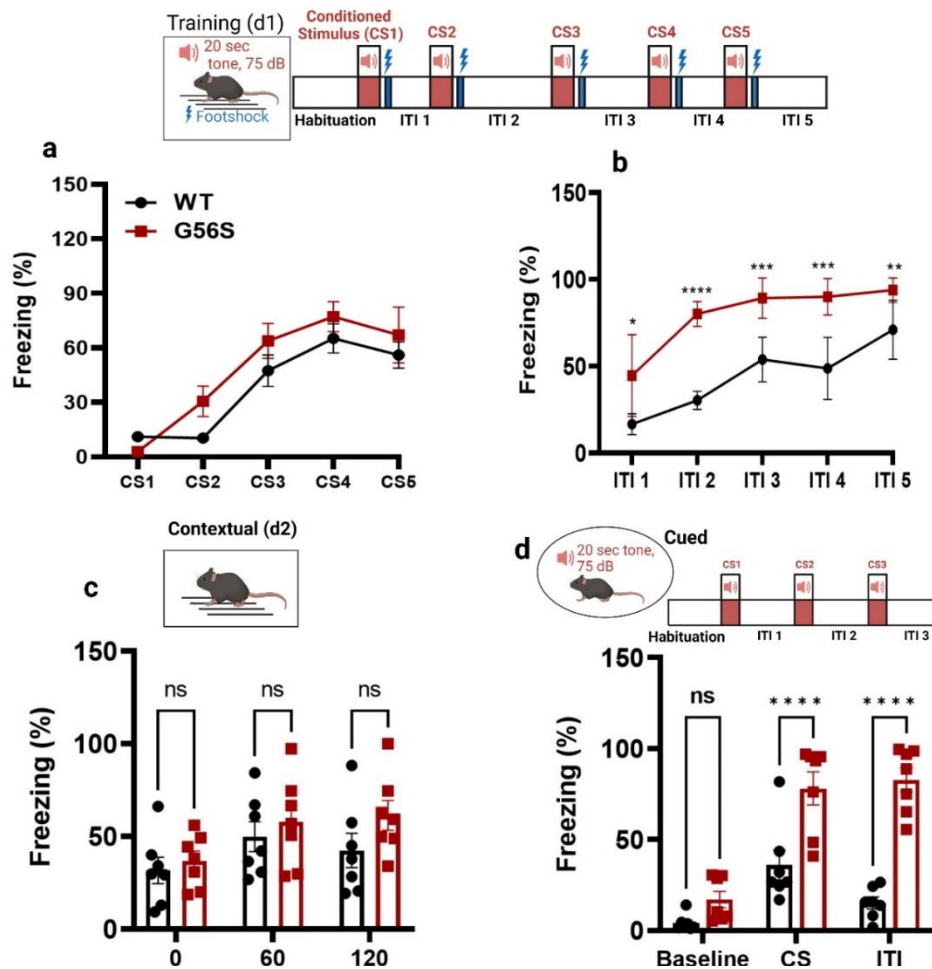
Figure 6. Auditory-cued fear responses following a conditioned stimulus (CS). (a) Fear learning and fear response levels after each conditioned stimulus (CS; inter-trial interval, ITI) were assessed in 4–5-month-old G56S and WT mice (n=7 per group). The fear response was expressed as the percentage of time spent in a stereotypical freezing state during the presentation of the CS repeated five times during fear acquisition (CS 1-5; a 75 dB tone lasting 20 sec followed by a foot shock). This was repeated four times with staggered inter-trial intervals. The inset documents the experimental sequences on day 1, which include habituation (hab), tone presentation (CS, loud-speaker symbol), shock delivery (lightning symbol), and ITIs of varying durations. (b) WT and G56S mice demonstrated significantly different responses during fear acquisition (genotype effects and genotype trial interactions were evaluated by two-way ANOVA for repeated measures). (c) Fear response in contextual setting, without sound and shock stimulation, performed 24 hours after fear acquisition. (d) Cue-fear response (with a changed environment) induced by CS alone (tone: 20 sec, repeated three times with no foot shock) with variable ITIs. The Baseline value represents the percentage spent in the freezing state during habituation before the CS (sound); the CS response represents the average of three CS trials; the bars labeled ITI represent the average of the three it is for each mouse. The inset documents the experimental sequences used on day 2, including habituation (hab), tone presentation (CS, loud-speaker symbol), and ITIs of varying durations. Results obtained from WT and G56S mice were compared using unpaired t-tests. Values shown are mean ± S.E.M. *$p < 0.05$; ** $p < 0.01$; ***$p < 0.001$; ****$p < 0.0001$.

G56S mice exhibit neuroanatomical changes

We explored brain anatomical structures to determine whether the G56S mutation and resulting alterations in polyamine metabolism were associated with major structural changes. We also determined how altered brain structures might correlate with the behavioral defects described in previous tests. For these experiments, brain volumes were assessed using T2-weighted anatomical scans and diffusion tensor imaging (DTI) (Figure 7a). Other DTI parameters

471   collected included fractional anisotropy (fa), mean diffusivity (md), axial diffusivity (ad), and

472   radial diffusivity (rd). The results of whole-brain imaging showed that the G56S mice have

473   significantly smaller brain volumes than WT mice (Figure 7b). Similarly, analysis of several

474   specific brain regions that were selected based on reports describing SRS patients (22,23) and

475   our behavioral data revealed that the volumes of the amygdala (involved in fear learning and

476   emotional responses), the hippocampus (involved in cognitive functions), and the corpus

477   callosum were all significantly lower in the G56S mouse strain (Figure 7c). Also, DTI analysis of

478   the various brain regions revealed that fa, which is a measure of the microstructural integrity of

479   the white matter of the amygdala and the corpus callosum, was significantly lower in the G56S

480   mice compared to the WT controls. The other regions, including the hippocampus and the

481   cortex, exhibited decreasing trends, although did not achieve statistically significant (Figure 7d).
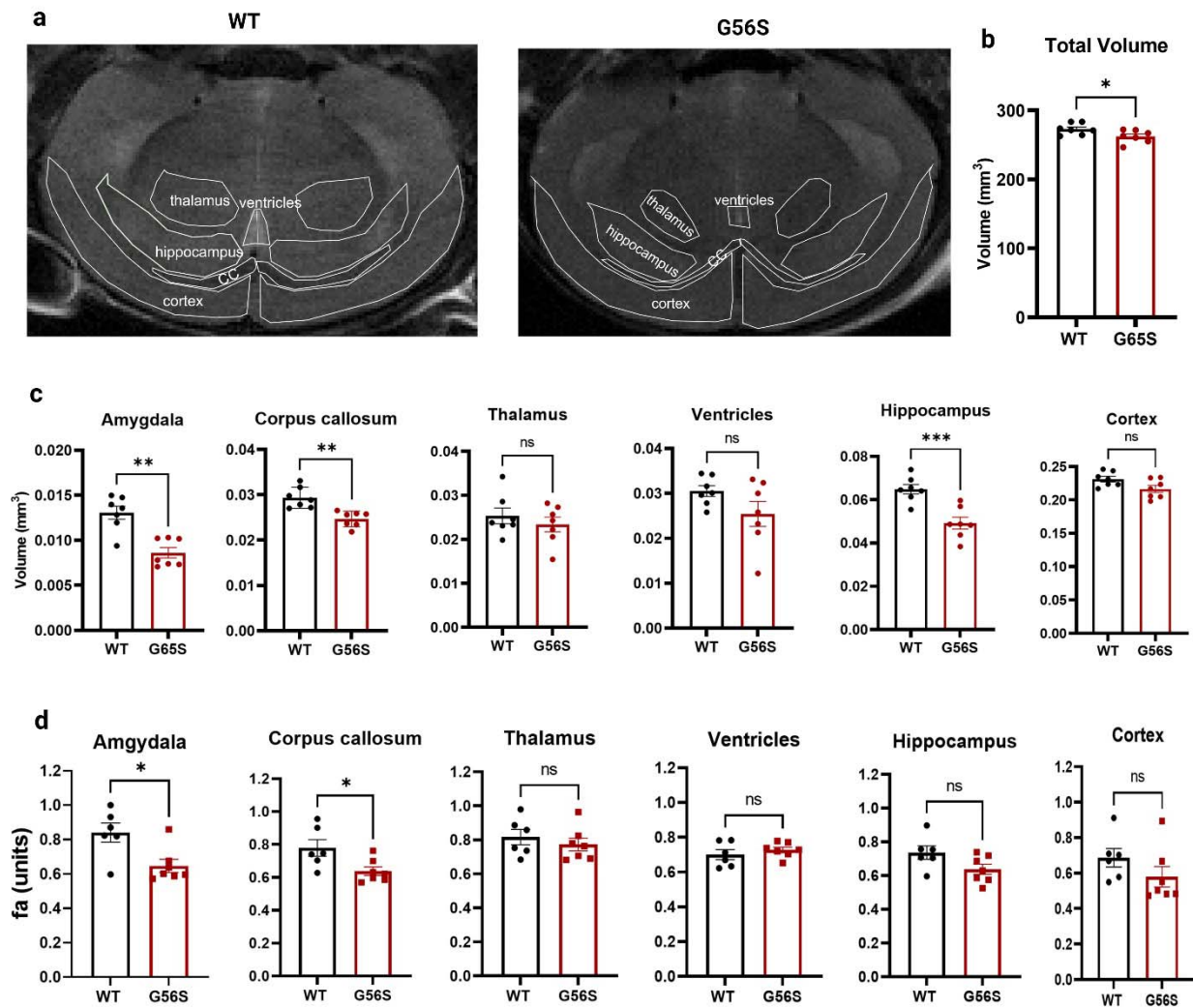
482

483   **Figure 7. *In vivo* MRI structural analyses.** (a) Representative MRI images of coronal sections of brains from WT
484   and G56S mice. Annotations of different regions of the brain were based on the Allen Mouse Brain Atlas. (b and c)
485   MRI volumetric analyses of the total brain volume and volumes of annotated regions highlighted in panel (a).
486   Quantification of the volume of each region was normalized to the total brain volume for each sample. Volumes of
487   each brain region were quantified using ITK snap software to assess RER8 MRI scan images. (d) Fractional

488 anisotropy (fa) was quantified using DSI studio software. Comparisons of single variables between WT and G56S
489 mice were performed using unpaired *t*-tests. Data shown are mean ± S.E.M. *$p < 0.05$; **$p < 0.01$; ***$p < 0.001$; ns,
490 not significant. **Note**: The amygdala region was not visible in the image shown in panel (a) above.

491 **Mutation in *Sms* gene alters transcriptomic profile of the G56S mouse brain cortex**

492 To elucidate the molecular mechanisms underlying some of the observed phenotypic and

493 behavioral differences, we isolated RNA and performed a transcriptomic analysis of the brain

494 cortex tissue of WT and G56S mice. We focused on the cortex because of its role in directing

495 higher complex tasks, including learning, memory, and consciousness. Furthermore, results

496 from previous studies suggest that spermine may have protective role specifically within the

497 cerebral cortex (22,27). The results of our transcriptomic analysis of brain cortex tissue from WT

498 and G56S mice revealed more than 1,000 differentially expressed genes (DEGs) (Figure 8a and

499 Supplementary **Table 2**). A heatmap revealed differential expression of genes involved in

500 several key cellular and metabolic processes (Figure 8b). Importantly we found differential

501 expression of genes that contribute to mitochondria function and ribosomal protein synthesis.

502 We performed gene enrichment pathway analysis to identify possible metabolic pathways that

503 might be altered in the G56S mice. Our results revealed that downregulation of genes involved

504 in mitochondrial oxidative phosphorylation and ribosomal protein synthesis (i.e., eukaryotic

505 initiation factor 2 [eIF2] signaling) in cortical tissue from the G56S mice (Figure 8c). In addition,

506 pathways involved in Huntington's disease, sirtuin, and synaptogenesis signaling pathways

507 were all upregulated in the G56S mice brain cortex compared to the WT (Figure 8c). The

508 expression pattern of genes involve in these metabolic processes were further confirmed in the

509 G56S mice relative to the WT by a Volcano plot (Figure 8d). Quantitative polymerase chain

510 reaction (qPCR) performed to validate the differential expression of genes associated with

511 mitochondrial oxidative phosphorylation confirmed decreased expression of *ATP5e, Uqcr10,*

512 *Cox6B1, Cox4i1, Cox7b, Ndufa4, and Ndufa7* as well as decreased expression of *Rpl17* and

513 *Rsp14* (both implicated in ribosome protein synthesis via eIF2 signaling) in the brain cortex of

514 G56S compared to WT mice (Figure 8e).

515 qPCR analysis also confirmed the observed upregulation of Huntington-associated protein 1,

516 *Hap1*, and the disease-related ionotropic NMDA receptor subunit 2b, *Grin2b* (Figure 8e).

517 Collectively, these data suggest that the G56S mutation in the *Sms* gene and alterations in

518 tissue polyamine levels resulted in specific changes in the expression profile of genes involved

519 in central cellular and metabolic processes of the brain. These observations may explain one or

520 more of the phenotypic abnormalities observed in G56S mice.

521
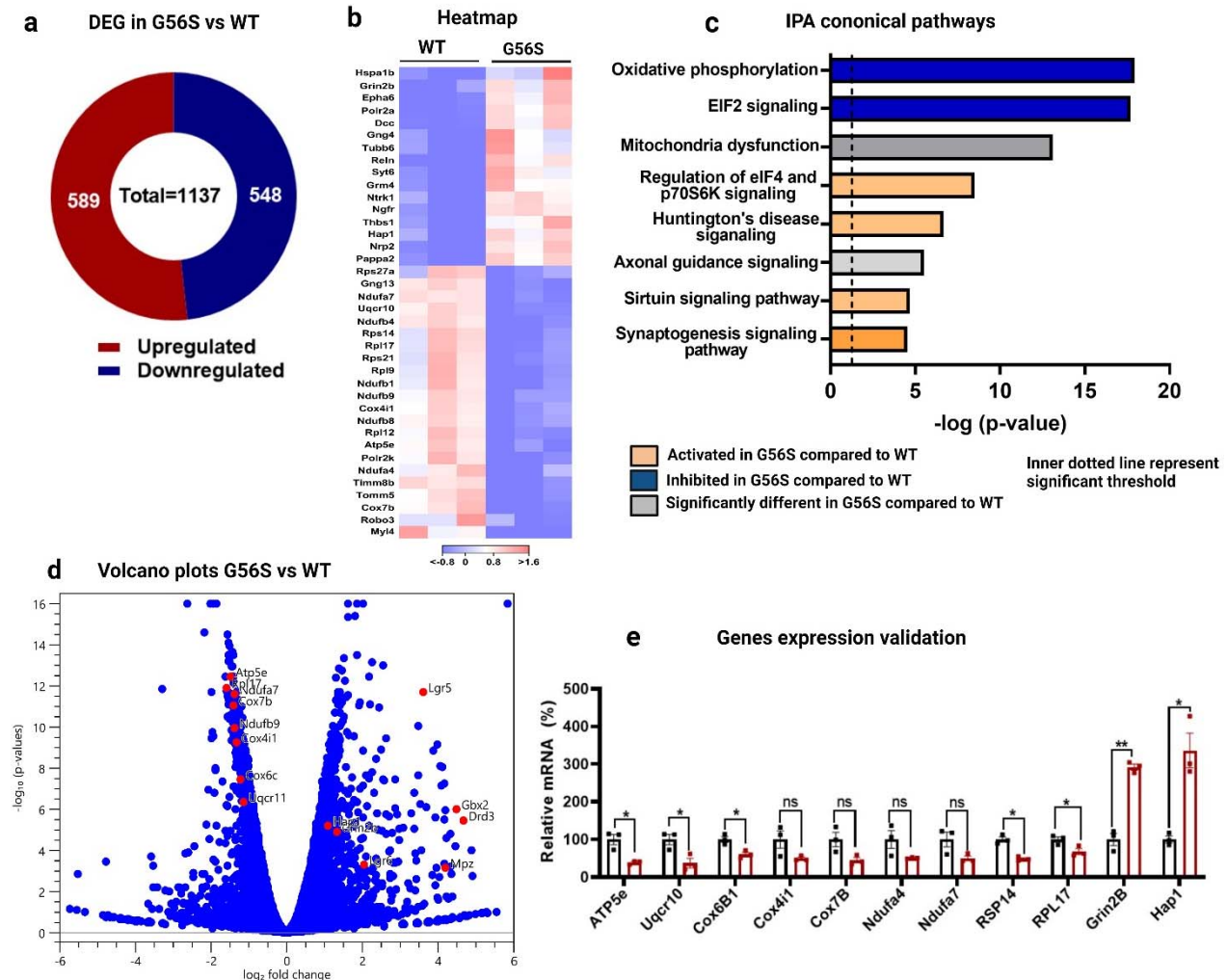
Figure 8. **Transcriptomic analysis of isolated brain cortical tissues**. (a) Differentially expressed genes (DEGs) were identified using Qiagen CLC Genomic Workshop software. (b) Heatmap of selected genes that exhibit statistically significant differences in expression ($p < 0.05$) and absolute values of $\log_2$-fold change (LFC) greater than or equal to 1. (c) Gene enrichment analysis of up- and downregulated transcripts with $p < 0.05$ and absolute LFC $\geq$ 0.5 in the brain tissue from G56S compared to WT mice. Gene enrichment analysis was done using the Qiagen Ingenuity Pathway Analysis (IPA) software. (d) A volcano plot showing the relative expression of selected genes involved in oxidative phosphorylation and other pathways based on the results of the enrichment analysis. (e) qPCR validation of RNA-seq results for selected genes implicated in oxidative phosphorylation, eukaryotic initiation factor 2 (eIF2) signaling, and Huntington's disease. Data shown are mean ± S.E.M, (n=3 for both WT and G56S mice). *p < 0.05; **p < 0.01, ns, not significant.

G56S mice exhibit impaired mitochondrial respiration

To confirm the downregulation of mitochondrial oxidative phosphorylation predicted by gene expression analysis, we isolated primary fibroblasts from both the WT and G56S mice and evaluated mitochondrial respiration using the XFe96 Seahorse bioanalyzer. Our results revealed that both basal and oligomycin-sensitive respiration rates were significantly diminished in fibroblasts isolated from G56S mice (Figures 9a and 9b). Similarly, maximum respiration and rates of ATP synthesis were also significantly reduced in fibroblasts from the G56S mice compared to the WT (Figures 9c and 9d). Taken together, these data suggest that SMS

542   deficiency and impaired polyamine metabolism in G56S fibroblasts will lead to impaired

543   mitochondrial bioenergetics and functions.

544
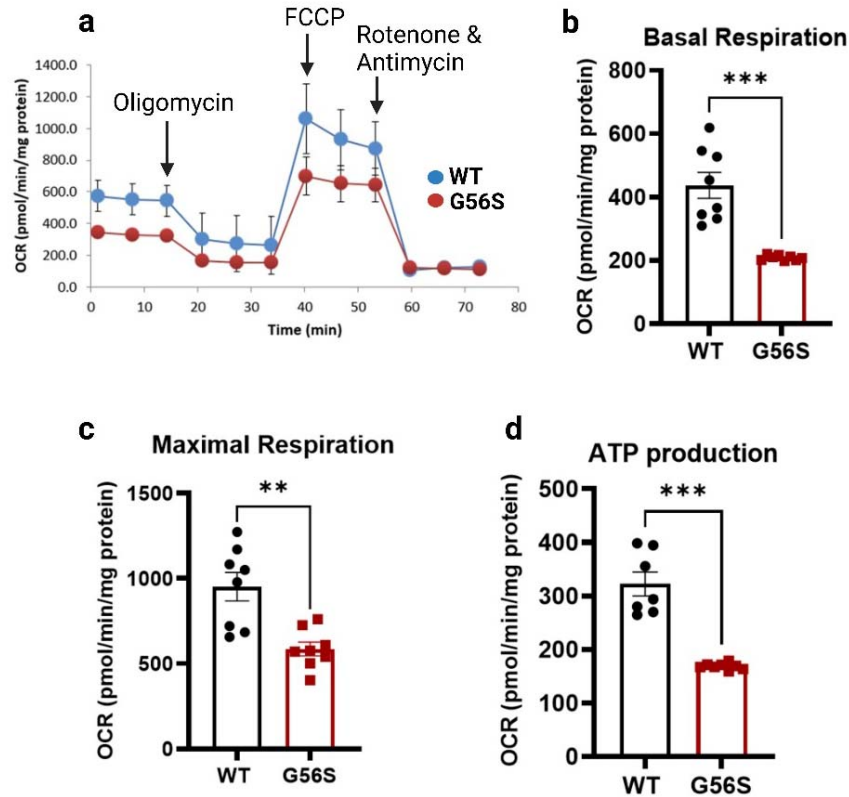
545
546   **Figure 9**. **Mitochondrial respiration in isolated fibroblasts**. (a) Respiratory profiles of primary fibroblasts isolated
547   from WT (blue line) and G56S (red). Oligomycin (ATP synthase inhibitor), FCCP (H$^+$ ionophore), and
548   rotenone/antimycin (mitochondria complex I/III inhibitors) were added at the times indicated. (b) Basal respiration, (c)
549   maximal respiration, and (d) ATP production in fibroblasts from WT and G56S mice were assessed using a Seahorse
550   XFe96 analyzer. Data shown are mean ± s.e.m. of average n=8 technical replicates of two independent experiments.
551   ***p < 0.01; ***p < 0.001.*

Discussion

553   One of the main challenges of preclinical research intended to elucidate the mechanisms

554   underlying rare brain-related disorders and other diseases associated with cognitive impairment

555   is the identification of robust and translationally-relevant behavioral phenotypes using animal

556   models. While the G56S mouse features an *Sms* gene-specific missense mutation that

557   replicates a genetic lesion identified in patients with severe form of SRS, however it is not

558   known whether this mouse represents a useful tool for therapeutic development. Therefore, the

559   goal of this study is to provide a detailed behavioral and neuroanatomical assessment of these

560   mice. We also studied the transcriptomic landscape of the brain cortex to identify gene

561   expression patterns that may contribute to the abnormalities observed in the mice and

562   conceivable in SRS patients.

SRS is a disease characterized by abnormal somatic features and a general failure to thrive. Patients are described as having asthenic body builds, mild short stature, and diminished body mass. These patients also exhibit abnormal bone structure and sustain frequent fractures (10). In the current study, we report that the G56S mice exhibit lower body weights as well as reduced overall length, bone mineral density, and body fat composition compared to their WT counterparts. These findings suggest that the G56S mouse model reproduces many of the abnormal clinical features described for SRS. However, the impact of the resulting disruptions in polyamine metabolism and their contributions to disease-specific symptomatology remain unknown. A previous study focused on bone marrow-derived multipotent stromal cells (MSCs) revealed that the mRNA silencing of SMS resulted in impaired cell proliferation and a reduced capacity for osteogenesis (28). These results suggest a possible link between the *Sms* mutation, dysregulated polyamine metabolism, and thus decreased bone mineral density in both patients and the G56S mice. While most SRS patients, including those with the G56S mutation (11) are eventually diagnosed with kyphoscoliosis, no scoliosis was detected in micro-CT scans of these mice. However, we cannot rule out the possibility that abnormal spines may develop in older mice.

The decreased body fat composition might be attributed to the increase in tissue spermidine, as this polyamine has been implicated in promoting lipolysis (29). However, it is also possible that the absence of SMS can result in impaired mitochondrial functions (15,28). In this case, the mice will depend more heavily on glycolysis as a means of energy generation; this will result in the utilization of greater amounts of food with less available to be converted to and stored as body fat. The decreased body weight seen in these mice supports the general idea that disturbances in polyamine homeostasis impair cell growth and tissue development (4) and lead to general growth failure.

Similar to what has been reported in many SRS patients, the G56S mouse displays signs of cognitive impairment and exhibits significant reductions in exploratory behavior when evaluated in an open field test. Collectively, these findings suggest that these mice exhibit amplified anxiety-related behaviors. This hypothesis was further confirmed using the fear conditioning test. Mice displayed significantly heightened fear responses when presented with an auditory conditioned stimulation (CS) followed by unconditioned stimulus (US; foot shock). The increase in fear responses in both the contextual and cued tests further confirm the observed heightened anxiety-related behavior in the G56S mouse strain. Overall, these data provide some evidence suggesting the existence of neurological abnormalities in these mice. Since polyamines are important contributors to the development of the nervous system (30), several regions of the

597　brain might be contributing to these behavioral defects. Both the amygdala and the
598　hippocampus in the G56S mice, which are brain regions involved in fear-associated memory
599　and learning, respectively, were decreased in volume compared to the WT, similar to that
600　reported in SRS patients (22). Thus, these results suggest that impaired polyamine metabolism
601　and toxic spermidine accumulation may lead to atrophy and neuronal loss in these regions (22)
602　as well as the defects in behavioral and learning outcomes observed in these mice. The
603　possibility that disrupted polyamine metabolism might lead to brain atrophy was further
604　confirmed by the decrease in the fa value found in G56S mice. Although we did not measure the
605　polyamine content in specific regions of the brain, we believe that the total brain polyamine
606　content most likely reflects the overall content in the different regions, given that G56S mice lack
607　SMS in all tissues and that this mutation is not tissue or brain-region specific.

608　Another potential mechanism that might explain the behavioral defects observed in G56S mice
609　is spermidine-mediated disruption of receptor signaling. In an earlier study, Rubin *et al.* (31)
610　reported that intra-amygdala administration of spermidine in an experimental rat model resulted
611　in a dose-dependent increase in freezing responses. These results suggested that the
612　accumulation of spermidine in the brains of G56S mice might contribute to the observed
613　increase in anxiety-related behaviors. The mechanisms underlying spermidine-mediated
614　increases in fear responses have not yet been clarified.

615　Spermidine may regulate the function of the amygdala via interactions with and modulation of
616　the ion channel receptor for N-methyl-D-aspartate (NMDA); earlier report detail polyamine-
617　mediated negative regulation of this receptor (32). Administration of arcaine, a putative
618　competitive antagonist at the polyamine binding site of the NMDA receptor, resulted in a
619　decrease in spermidine-induced fear responses in rats (31). Collectively, these results suggest
620　that spermidine levels may have an impact on amygdala function and that accumulation of
621　spermidine may induce a fear response as well as other behavioral abnormalities seen in the
622　G56S mice. It is important to note that anxiety has been identified as one of the main symptoms
623　of numerous neurological disorders (33). Although there are no clinical reports that document
624　this specific behavior in SRS patients, family members have confirmed anxiety and the
625　prevalence of fear-related behaviors in some patients (Personal communication, Snyder-
626　Robinson Foundation conference 2022)

627　In addition to the neuroanatomic defects, other potential mechanisms contributing to the
628　phenotypic abnormalities observed in the G56S mice were revealed by the transcriptomic
629　analysis. These include impaired mitochondrial function, alterations in ribosomal protein
630　synthesis signaling pathways, and upregulation of genes implicated in the pathogenesis of

631 Huntington's disease. The mitochondria are important energy-generating cellular organelles;
632 mitochondrial dysfunction has been implicated in a variety of different neurological or
633 neurodegenerative diseases (34). Results from several previous studies have suggested that
634 impaired mitochondrial function might contribute to the pathogenesis of SRS (15,28) via one of
635 several potential mechanisms:

636 (i) Increased spermidine levels that accumulate in cells that lack SMS may promote the
637 synthesis and release of reactive oxygen species (ROS) secondary to increased
638 catabolism. Elevated ROS results in mitochondrial oxidative stress and impaired
639 mitochondrial function (15).

640 (ii) Polyamines play essential roles in modulating gene expression. Earlier reports
641 suggest that spermine modulates mammalian mitochondrial translation initiation
642 processes (35,36). Thus, the lack of SMS or spermine could inhibit synthesis of
643 mitochondrial proteins and result in impaired mitochondrial functions.

644 (iii) Normal mitochondrial metabolism can result in the accumulation of potentially
645 damaging levels of by-products including ROS and Ca^{2+} (37). As a polycationic
646 molecule, spermine can scavenge mitochondrial ROS (38,39), and reduce the levels
647 of mitochondrial permeability transition pore (mPTP) generated in response to Ca^{2+}
648 accumulation (40). Thus, the lack of SMS or an observed decrease in cellular
649 spermine content may result in mitochondrial damage.

650 (iv) Another potential mechanism of mitochondrial impairment in SRS may relate to the
651 decreased expression of nuclear genes encoding mitochondrial proteins reported in
652 this study. Although we do not yet understand how SMS mutations and/or altered
653 spermine concentrations result in the changes in gene expression observed, either
654 factor may be involved in direct or indirect interactions with critical transcription
655 factors. It will be important to identify relevant transcription factors as this may
656 improve our understanding of how spermine and/or SMS modulate mitochondrial
657 function.

658 In conclusion, efforts to develop effective therapies for SRS will require a better understanding
659 of the disease pathophysiology as well as suitable disease-specific animal models that
660 recapitulate many of the critical abnormalities diagnosed in these patients. The findings
661 presented in this study suggest that the G56S mouse is a good model that can be used to study
662 SRS pathogenesis and may be an important tool for therapeutic development. This study also
663 provides parameters that may be used to assess the effectiveness of therapy for SRS in a

664 murine model. Finally, the data shown here offers some insights that could be used to improve
665 the current clinical management of SRS.

666

667 **Acknowledgements**:

678 **Author contributions:**

679 Conceptualization: O.A. and D.U.K; Investigation: O.A., A.M., M.J., M.E.P., Y.G., Y.W., J.F.,
680 T.M.S, R.A.C.; Formal analysis and visualization: O.A., A.M., M.E.P., Y.G., Y.W., H.B., D.U.K;
681 Writing: O.A. and D.U.K.; Supervision, D.U.K.

682 **References**:

683 1.   Bachrach U, Wang YC, Tabib A. Polyamines: New cues in cellular signal transduction. News in
684   Physiological Sciences. 2001;16(3).

685 2.   Landau G, Bercovich Z, Park MH, Kahana C. The role of polyamines in supporting growth of
686   mammalian cells is mediated through their requirement for translation initiation and elongation.
687   Journal of Biological Chemistry. 2010;285(17).

688 3.   Hesterberg R, Cleveland J, Epling-Burnette P. Role of Polyamines in Immune Cell Functions.
689   Medical Sciences. 2018;6(1).

690 4.   Kemaladewi DU, Benjamin JS, Hyatt E, Ivakine EA, Cohn RD. Increased polyamines as protective
691   disease modifiers in congenital muscular dystrophy. Hum Mol Genet. 2018;27(11).

692 5.   Akinyele O, Wallace HM. Understanding the Polyamine and mTOR Pathway Interaction in Breast
693   Cancer Cell Growth. Medical Sciences. 2022 Sep 10;10(3):51.

694 6.   Arruabarrena-Aristorena A, Zabala-Letona A, Carracedo A. Oil for the cancer engine: The cross-
695   talk between oncogenic signaling and polyamine metabolism. Vol. 4, Science Advances. 2018.

696   7.   Lewandowski NM, Ju S, Verbitsky M, Ross B, Geddie ML, Rockenstein E, et al. Polyamine pathway
697   contributes to the pathogenesis of Parkinson disease. Proc Natl Acad Sci U S A. 2010;107(39).

698   8.   Soda K. The mechanisms by which polyamines accelerate tumor spread. Journal of Experimental
699   and Clinical Cancer Research. 2011;30(1).

700   9.   Milovic V, Turchanowa L. Polyamines and colon cancer. In: Biochemical Society Transactions.
701   2003.

702   10.   Schwartz CE, Peron A, Kutler MJ, Snyder-Robinson Syndrome ;, Adam MP, Ardinger HH, et al.
703   Snyder-Robinson Syndrome Synonym: Spermine Synthase Deficiency. 2013.

704   11.   de Alencastro G, McCloskey DE, Kliemann SE, Maranduba CMC, Pegg AE, Wang X, et al. New SMS
705   mutation leads to a striking reduction in spermine synthase protein function and a severe form of
706   Snyder-Robinson X-linked recessive mental retardation syndrome. J Med Genet. 2008;45(8).

707   12.   Larcher L, Norris JW, Lejeune E, Buratti J, Mignot C, Garel C, et al. The complete loss of function
708   of the SMS gene results in a severe form of Snyder-Robinson syndrome. Eur J Med Genet.
709   2020;63(4).

710   13.   Valera Ribera C, Martinez-Ferrer, Flores Fernández E, Vázquez Gómez I, Orenes Vera A, Valls
711   Pascual E, et al. Snyder-Robinson syndrome: differential diagnosis of osteogenesis imperfecta.
712   Osteoporosis International. 2022;33(5).

713   14.   Cason AL, Ikeguchi Y, Skinner C, Wood TC, Holden KR, Lubs HA, et al. X-linked spermine synthase
714   gene (SMS) defect: The first polyamine deficiency syndrome. European Journal of Human
715   Genetics. 2003;11(12).

716   15.   Li C, Brazill JM, Liu S, Bello C, Zhu Y, Morimoto M, et al. Spermine synthase deficiency causes
717   lysosomal dysfunction and oxidative stress in models of Snyder-Robinson syndrome. Nat
718   Commun. 2017;8(1).

719   16.   Tao X, Zhu Y, Diaz-Perez Z, Yu SH, Foley JR, Stewart TM, et al. Phenylbutyrate modulates
720   polyamine acetylase and ameliorates Snyder-Robinson syndrome in a Drosophila model and
721   patient cells. 2022; Available from: https://doi.org/10.1172/jci.

722   17.   MacKintosh CA, Pegg AE. Effect of spermine synthase deficiency on polyamine biosynthesis and
723   content in mice and embryonic fibroblasts, and the sensitivity of fibroblasts to 1,3-bis-(2-
724   chloroethyl)-N-nitrosourea. Biochemical Journal. 2000;351(2).

725   18.   Wang X, Ikeguchi Y, McCloskey DE, Nelson P, Pegg AE. Spermine synthesis is required for normal
726   viability, growth, and fertility in the mouse. Journal of Biological Chemistry. 2004;279(49).

727   19.   Meyer RA, Henley CM, Meyer MH, Morgan PL, McDonald AG, Mills C, et al. Partial deletion of
728   both the spermine synthase gene and the Pex gene in the X-linked hypophosphatemic, Gyro (Gy)
729   mouse. Genomics. 1998;48(3).

730   20.   Lyon MF, Scriver CR, Baker LR, Tenenhouse HS, Kronick J, Mandla S. The Gy mutation: Another
731   cause of X-linked hypophosphatemia. Proc Natl Acad Sci U S A. 1986;83(13).

732   21.   Laskowski S. THE JACKSON LABORATORY AND SNYDER-ROBINSON FOUNDATION ANNOUNCE
733   NEW RESEARCH MODELS FOR SNYDER-ROBINSON SYNDROME.

734   22.   Kesler SR, Schwartz C, Stevenson RE, Reiss AL. The impact of spermine synthase (SMS) mutations
735   on brain morphology. Neurogenetics. 2009;10(4).

736   23.   Starks RD, Kirby PA, Ciliberto MA, Hefti MM. Snyder-Robinson Syndrome: An Autopsy Case
737   Report. Autops Case Rep. 2018;8(3).

738   24.   Tsien JZ, Huerta PT, Tonegawa S. The essential role of hippocampal CA1 NMDA receptor-
739   dependent synaptic plasticity in spatial memory. Cell. 1996;87(7).

740   25.   Khan M, Gasser S. Generating primary fibroblast cultures from mouse ear and tail tissues. Journal
741   of Visualized Experiments. 2016;2016(107).

742   26.   Kabra PM, Lee HK, Lubich WP, Marton LJ. Solid-phase extraction and determination of dansyl
743   derivatives of unconjugated and acetylated polyamines by reversed-phase liquid
744   chromatography: Improved separation systems for polyamines in cerebrospinal fluid, urine and
745   tissue. J Chromatogr B Biomed Sci Appl. 1986;380(C).

746   27.   Clarkson AN, Liu H, Pearson L, Kapoor M, Harrison JC, Sammut IA, et al. Neuroprotective effects
747   of spermine following hypoxia-ischemia-induced brain damage: A mechanistic study. The FASEB
748   Journal. 2004 Jul 7;18(10):1114–6.

749   28.   Ramsay AL, Alonso-Garcia V, Chaboya C, Radut B, Le B, Florez J, et al. Modeling Snyder-Robinson
750   Syndrome in multipotent stromal cells reveals impaired mitochondrial function as a potential
751   cause for deficient osteogenesis. Sci Rep. 2019;9(1).

752   29.   Monelli E, Villacampa P, Zabala-Letona A, Martinez-Romero A, Llena J, Beiroa D, et al. Angiocrine
753   polyamine production regulates adiposity. Nat Metab. 2022;4(3).

754   30.   Slotkin TA, Bartolome J. Role of ornithine decarboxylase and the polyamines in nervous system
755   development: A review. Brain Res Bull. 1986;17(3).

756   31.   Rubin MA, Berlese DB, Stiegemeier JA, Volkweis MA, Oliveira DM, dos Santos TLB, et al. Intra-
757   Amygdala Administration of Polyamines Modulates Fear Conditioning in Rats. Journal of
758   Neuroscience. 2004;24(9).

759   32.   Subramaniam S, O'connor MJ, Masukawa LM, McGonigle P. Polyamine effects on the NMDA
760   receptor in human brain. Exp Neurol. 1994;130(2).

761   33.   Davies RD, Gabbert SL, Riggs PD. Anxiety disorders in neurologic illness. Curr Treat Options
762   Neurol. 2001;3(4).

763   34.   Guo CY, Sun L, Chen XP, Zhang DS. Oxidative stress, mitochondrial damage and
764   neurodegenerative diseases. Neural Regen Res. 2013;8(21).

765   35.   Lee M, Matsunaga N, Akabane S, Yasuda I, Ueda T, Takeuchi-Tomita N. Reconstitution of
766   mammalian mitochondrial translation system capable of correct initiation and long polypeptide
767   synthesis from leaderless mRNA. Nucleic Acids Res. 2021;49(1).

768   36.   Christian BE, Haque ME, Spremulli LL. The effect of spermine on the initiation of mitochondrial
769   protein synthesis. Biochem Biophys Res Commun. 2010;391(1).

770   37.   Zorov DB, Juhaszova M, Sollott SJ. Mitochondrial reactive oxygen species (ROS) and ROS-induced
771   ROS release. Vol. 94, Physiological Reviews. 2014.

772   38.   Ha HC, Sirisoma NS, Kuppusamy P, Zweier JL, Woster PM, Casero RA. The natural polyamine
773   spermine functions directly as a free radical scavenger. Proc Natl Acad Sci U S A. 1998;95(19).

774   39.   Sava IG, Battaglia V, Rossi CA, Salvi M, Toninello A. Free radical scavenging action of the natural
775   polyamine spermine in rat liver mitochondria. Free Radic Biol Med. 2006;41(8).

776   40.   Elustondo PA, Negoda A, Kane CL, Kane DA, Pavlov E v. Spermine selectively inhibits high-
777   conductance, but not low-conductance calcium-induced permeability transition pore. Biochim
778   Biophys Acta Bioenerg. 2015;1847(2).

779

780